Lepton flavor violation in Higgs boson decays at the HL-LHC

M. A. Arroyo-Ureña, 1,2,* E. A. Herrera-Chacón, 3,† Iran Melendez-Hernández, 1,2,‡ and S. Rosado-Navarro 2, §

¹Facultad de Ciencias Físico-Matemáticas,
Benemérita Universidad Autónoma de Puebla, C.P. 72570, Puebla, México,
²Centro Interdisciplinario de Investigación y Enseñanza de la Ciencia (CIIEC),
Benemérita Universidad Autónoma de Puebla, C.P. 72570, Puebla, México,

³Institute for Particle Physics Phenomenology,
Durham University, South Road, Durham, DH1 3LE

Abstract

We investigate the prospects for discovering lepton flavor-violating Higgs decays in proton-proton collisions, focusing on $h \to \ell_i \ell_j$ ($\ell_i \neq \ell_j$, $\ell = e, \mu, \tau$). The analysis is carried out within a Froggatt-Nielsen model, which provides a natural mechanism for such processes. By scanning the phenomenologically viable parameter space, we identify scenarios that yield observable signals at the High-Luminosity LHC (HL-LHC). For an integrated luminosity of 2400 fb⁻¹, we project that $h \to e\mu$ could reach the 5σ discovery threshold, while $h \to \tau \mu$ may achieve about 4σ . We also obtain 2σ exclusion limits of $\mathcal{BR}(h \to e\mu) \lesssim 4.3 \times 10^{-6}$ and $\mathcal{BR}(h \to \tau \mu) \lesssim 5.2 \times 10^{-5}$. These findings underscore the HL-LHC's unique sensitivity to probe new physics through rare Higgs decays.

^{*} marco.arroyo@fcfm.buap.mx

[†] edwin.a.herrera-chacon@durham.ac.uk

[‡] iran.melendezh@alumno.buap.mx

[§] sebastian.rosado@protonmail.com

I. INTRODUCTION

Lepton Flavor Violation (LFV) refers to transitions between the charged lepton families—e, μ , and τ —that do not conserve lepton family number. In the Standard Model (SM) with massless neutrinos, these individual lepton numbers are strictly conserved. While the introduction of non-zero neutrino masses allows for such processes, their expected rates are highly suppressed by factors of m_{ν}^2/m_W^2 [1], rendering them exceptionally sensitive probes of Beyond the SM (BSM) physics.

The phenomenon of neutrino oscillations, a direct quantum mechanical consequence of non-zero neutrino masses and mixing, provides an established manifestation of LFV in the neutral sector. This has been convincingly demonstrated by experiments utilizing solar, atmospheric, reactor, and accelerator neutrinos [2–5], confirming the theoretical foundations laid out in [6, 7].

In contrast, the observation of Charged Lepton Flavor-Violating (CLFV) decays would represent an unambiguous signature of new physics. To date, no evidence has been found for processes such as the lepton decays $\tau^- \to e^- e^- e^+$, $\tau^- \to \mu^- \mu^- \mu^+$ [8], and $\mu^- \to e^- e^- e^+$ [9], or the radiative decays $\mu \to e\gamma$ [10], $\tau \to \mu\gamma$, and $\tau \to e\gamma$ [11]. These searches have resulted in very stringent upper limits on the corresponding branching ratios.

A particularly compelling LFV process is the Higgs boson decay $h \to \tau \mu$, initially investigated in [12–14] and analyzed its potential detectability in [15, 16]. This decay has been extensively explored within several SM extensions, including models with massive neutrinos, extended scalar, and supersymmetric models [17–21]. Less studied have been the processes $h \to \tau e$ and $h \to e \mu$, which have a special interest in this work.

Current experimental upper limits on these channels, as reported by the CMS and ATLAS collaborations [22, 23], exhibit the values $\mathcal{BR}(h \to \tau \mu) < 1.5 \times 10^{-3}$, $\mathcal{BR}(h \to \tau e) < 2 \times 10^{-3}$, and $\mathcal{BR}(h \to e\mu) < 4.4 \times 10^{-5}$. Although these limits are not yet highly restrictive, they establish a baseline for future searches for the $h \to \ell_i \ell_j$ decays with integrated luminosities larger than the one reached by the LHC (300 fb⁻¹). This could be achieved at the HL-LHC [24], which will represent a new stage of the LHC expected to begin around 2026 with a center-of-mass energy of 14 TeV. The upgrade aims at increasing the integrated luminosity by a factor of ten (3000 fb⁻¹, around the year 2035) with respect to the final stage of the LHC.

This work investigates the decays $h \to \ell_i \ell_j$ within a theoretical framework that extends the SM scalar sector with a complex singlet and incorporates the Froggatt-Nielsen mechanism [25], which provides a potential explanation for the hierarchical structure of fermion masses and mixings. We explore realistic benchmark points (BP) in the model's parameter space which yield different production cross sections and, consequently, different projected significances, making them prime targets for investigation at the HL-LHC.

This work is structured as follows. In Sec. II, we conduct a comprehensive review of the Froggatt-Nielsen Singlet Model (FNSM). Experimental and theoretical constraints on the model parameter space are also included. Section III focuses on taking advantage of the insights gained from the previous section, performing a computational analysis of the proposed signal and its SM

background processes. Finally, the conclusions are presented in Sec. IV.

II. THEORETICAL FRAMEWORK

In this section we present the relevant theoretical aspects of the FNSM. In Refs. [26–35] a deep theoretical analysis of the model and a study on the model parameter space are also reported.

A. Scalar sector

The scalar sector is extended by adding a complex singlet scalar field, S_F , to the Standard Model (SM). In the unitary gauge, the SM Higgs doublet Φ and the new singlet S_F are expressed as:

$$\Phi = \begin{pmatrix} 0 \\ \frac{v + \phi^0}{\sqrt{2}} \end{pmatrix}, \quad S_F = \begin{pmatrix} \frac{v_s + S_R + iS_I}{\sqrt{2}} \end{pmatrix},$$

where v_s and v denote the vacuum expectation values (VEVs) of the Higgs doublet and the complex singlet, respectively. The scalar potential is required to be invariant under a flavor-dependent $U(1)_F$ symmetry, under which the fields transform as $\Phi \to \Phi$ and $S_F \to e^{i\alpha}S_F$. In the general FNSM, the scalar potential allows for a complex VEV for the singlet $\langle S_F \rangle_0 = \frac{v_s}{\sqrt{2}}e^{i\xi}$. However, for this work, we restrict our analysis to the CP-conserving scenario by setting the phase $\xi = 0$.

The CP-conserving scalar potential is then given by:

$$V_0 = -\frac{1}{2}m_1^2 \Phi^{\dagger} \Phi - \frac{1}{2}m_2^2 S_F^* S_F + \frac{1}{2}\lambda_1 (\Phi^{\dagger} \Phi)^2 + \lambda_2 (S_F^* S_F)^2 + \lambda_3 (\Phi^{\dagger} \Phi) (S_F^* S_F). \tag{2.1}$$

After spontaneous symmetry breaking (SSB), driven by the VEVs of Φ and S_F , a massless Goldstone boson emerges. To generate a mass for this state, we introduce a soft U(1)F-breaking term to the scalar potential in Eq. (2.1):

$$V \text{soft} = -\frac{1}{2}m_3^2(S_F^2 + S_F^{*2}). \tag{2.2}$$

The complete scalar potential of the model is therefore

$$V_{\text{FNSM}} = V_0 + V_{\text{soft}}.$$
 (2.3)

Following SSB and the application of the minimization conditions to the potential V_{FNSM} are performed, the mixing between the ϕ^0 and S_R fields, induced by the λ_3 parameter, leads to the following relations for the mass parameters:

$$m_1^2 = v^2 \lambda_1 + v_s^2 \lambda_3, \tag{2.4}$$

$$m_2^2 = -2m_3^2 + 2v_s^2 \lambda_2 + v^2 \lambda_3. (2.5)$$

These parameters define the scalar mass matrix. Furthermore, the soft $U(1)_F$ -breaking term V_{soft} explicitly generates a mass for the pseudo-scalar Flavon field S_I .

Since all parameters in the potential (2.1) are real, the resulting mass matrix is block-diagonal, and the CP-even and CP-odd scalar sectors do not mix. In the (ϕ_0, S_R) basis, the CP-even mass matrix is given by

$$M_S^2 = \begin{pmatrix} \lambda_1 v^2 & \lambda_3 v v_s \\ \lambda_3 v v_s & 2\lambda_2 v_s^2 \end{pmatrix}.$$

The mass eigenstates are obtained through the standard 2×2 rotation:

$$\begin{pmatrix} \phi^0 \\ S_R \end{pmatrix} = \begin{pmatrix} \cos \alpha & \sin \alpha \\ -\sin \alpha & \cos \alpha \end{pmatrix} \begin{pmatrix} h \\ H_F \end{pmatrix},$$

where we identify h as the SM-like Higgs boson and H_F is the CP-even Flavon. The CP-odd Flavon is associated with the imaginary part of the complex singlet: $S_I \equiv A_F$ with mass $M_{A_F}^2 = 2m_3^2$. The physical masses M_{ϕ} ($\phi = h, H_F, A_F$) are related to the parameters of the scalar potential in Eq.(2.1) as follows:

$$\lambda_{1} = \frac{(\cos \alpha M_{h})^{2} + (\sin \alpha M_{H_{F}})^{2}}{v^{2}},$$

$$\lambda_{2} = \frac{M_{A_{F}}^{2} + (\cos \alpha M_{H_{F}})^{2} + (\sin \alpha M_{h})^{2}}{2v_{s}^{2}},$$

$$\lambda_{3} = \frac{\cos \alpha \sin \alpha}{vv_{s}} (M_{H_{F}}^{2} - M_{h}^{2}).$$
(2.6)

B. Yukawa Lagrangian

The Yukawa Lagrangian, invariant under the $U(1)_F$ symmetry, is given by [25]:

$$\mathcal{L}_{Y} = \rho_{ij}^{d} \left(\frac{S_{F}}{\Lambda}\right)^{q_{ij}^{d}} \bar{Q}_{i} d_{R_{j}} \Phi + \rho_{ij}^{u} \left(\frac{S_{F}}{\Lambda}\right)^{q_{ij}^{u}} \bar{Q}_{i} u_{R_{j}} \tilde{\Phi}$$

$$+ \rho_{ij}^{\ell} \left(\frac{S_{F}}{\Lambda}\right)^{q_{ij}^{\ell}} \bar{L}_{i} \ell_{R_{j}} \Phi + \rho_{ij}^{\nu} \left(\frac{S_{F}}{\Lambda}\right)^{q_{ij}^{\nu}} \bar{L}_{i} \nu_{R_{j}} \tilde{\Phi} + \text{h.c.}, \qquad (2.7)$$

where ρ_{ij}^f $(f = u, d, \ell, \nu)$ are $\mathcal{O}(1)$ dimensionless couplings, q_{ij}^f are the flavor charges chosen to reproduce the observed fermion mass hierarchy, and Λ is the ultraviolet cutoff scale.

After SSB of the $U(1)_F$ and electroweak symmetries, the Lagrangian in Eq. (2.7) generates the effective Yukawa couplings. By considering the unitary gauge and making the expansion of the neutral component of the heavy Flavon S_F around its VEV v_s , one obtains:

$$\left(\frac{S_F}{\Lambda}\right)^{q_{ij}} \simeq \left(\frac{v_s}{\sqrt{2}\Lambda}\right)^{q_{ij}} \left[1 + q_{ij}\left(\frac{S_R + iS_I}{v_s}\right)\right],$$
(2.8)

From Eqs. (2.7), (2.8) and after replacing the mass eigenstates, the Yukawa Lagrangian reads:

$$\mathcal{L}_{Y} = \frac{1}{v} [\bar{U}M^{u}U + \bar{D}M^{d}D + \bar{L}M^{\ell}L](\cos\alpha h + \sin\alpha H_{F})$$

$$+ \frac{v}{\sqrt{2}v_{s}} [\bar{U}_{i}\tilde{Z}_{ij}^{u}U_{j} + \bar{D}_{i}\tilde{Z}_{ij}^{d}D_{j} + \bar{L}_{i}\tilde{Z}_{ij}^{\ell}L_{j}]$$

$$\times (-\sin\alpha h + \cos\alpha H_{F} + iA_{F}) + \text{h.c.}, \qquad (2.9)$$

where the Higgs-Flavon couplings are encapsulated in the $\tilde{Z}_{ij}^f = U_L^f Z_{ij}^f U_L^{f\dagger}$ matrix elements and M^f corresponds to the diagonal fermion mass matrix. The couplings \tilde{Z}_{ij}^f can be written as follows

$$\tilde{Z}_{ij}^f = \tilde{\rho}_{ij}^f \left(\frac{v_s}{\sqrt{2}\Lambda}\right)^{q_{ij}^f},\tag{2.10}$$

where $\tilde{\rho}_{ij}^f$ encompasses the diagonalization effects of Z_{ij}^f into ρ_{ij}^f . This means that, in general, $\tilde{\rho}_{ij}^f$ is different from $\mathcal{O}(1)$. Equation (2.10) remains nondiagonal even after the process of diagonalization of the mass matrices, as a consequence the FNSM allows for flavor-changing neutral currents. The exponents q_{ij}^f are determined by the flavor charges of the fermions and the Higgs doublet. For the quark sector, they are given by [29]:

$$q_{ij}^{d} = q_{Q_i} - q_{d_j} - q_H,$$

$$q_{ij}^{u} = q_{Q_i} - q_{u_j} + q_H,$$
(2.11)

where $q_{u_i} = q_{u,c,t}$ and $q_{d_i} = q_{d,s,b}$ are the flavor charges of the right-handed quark singlets, q_{Q_i} are the charges of the quark doublets, and q_H is the Higgs doublet charge. To reproduce the measured quark masses, the charges are fixed to $q_S = +1$, $q_H = 0$ and

$$\begin{pmatrix} q_{Q_1} & q_{Q_2} & q_{Q_3} \\ q_u & q_c & q_t \\ q_d & q_s & q_b \end{pmatrix} = \begin{pmatrix} 3 & 2 & 0 \\ -5 & -2 & 0 \\ -4 & -3 & -3 \end{pmatrix}$$

The analogous expressions for the lepton sector in Eq. (2.10) are given by

$$q_{ij}^{\ell} = q_{L_i} - q_{\ell_j} - q_H,$$

$$q_{ij}^{\nu} = q_{L_i} - q_{\nu_i} + q_H,$$
(2.12)

where $q_{\nu_j} = q_{\nu_e}$, $q_{\nu_{\mu}}$, $q_{\nu_{\tau}}$ and $q_{\ell_j} = q_e$, q_{μ} , q_{τ} are the flavor charges of the right-handed neutrino and charged lepton singlets, respectively, and q_{L_i} are the charges of the lepton doublets. The specific charge assignments chosen to reproduce the observed lepton masses and mixing pattern are:

$$\begin{pmatrix} q_{L_1} & q_{L_2} & q_{L_3} \\ q_{\nu_e} & q_{\nu_{\mu}} & q_{\nu_{\tau}} \\ q_e & q_{\mu} & q_{\tau} \end{pmatrix} = \begin{pmatrix} 1 & 0 & 0 \\ -24 & -21 & -20 \\ -8 & -5 & -3 \end{pmatrix}$$

With the definition $\epsilon = v_s/\sqrt{2}\Lambda$, the fermion mass matrices exhibit the following hierarchy:

$$\frac{m_b}{m_t} \approx \epsilon^3, \ \frac{m_c}{m_t} \approx \epsilon^4, \ \frac{m_s}{m_t} \approx \epsilon^5, \ \frac{m_d}{m_t} \approx \epsilon^7, \ \frac{m_u}{m_t} \approx \epsilon^8
\frac{m_\tau}{m_t} \approx \epsilon^3, \ \frac{m_\mu}{m_t} \approx \epsilon^5, \ \frac{m_e}{m_t} \approx \epsilon^9, \ m_t \approx \frac{v}{\sqrt{2}},$$
(2.13)

and the CKM matrix becomes

$$V_{\rm CKM} pprox \left(egin{array}{ccc} 1 & \epsilon & \epsilon^3 \ \epsilon & 1 & \epsilon^2 \ \epsilon^3 & \epsilon^2 & 1 \end{array}
ight).$$

As far as the ϕVV (V=W,Z) interactions are concerned, from the kinetic terms of the Higgs doublet and the complex singlet we can extract their couplings. Thus, we present the relevant Feynman rules in Table I.

Vertex (ϕXX) Coupling constant $(g_{\phi}XX)$		
$hf_iar{f}_j$	$rac{c_{lpha}}{v} ilde{M}_{ij}^f-s_{lpha}r_s ilde{Z}_{ij}^f$	
$H_F f_i ar{f}_j$	$\frac{s_{lpha}}{v} ilde{M}_{ij}^f + c_{lpha}r_s ilde{Z}^{f_{ij}}$	
$A_F f_i \bar{f}_j$	$r_s ilde{Z}^{f_{ij}}$	
hZZ	$rac{gM_Z}{c_W}c_{lpha}$	
hWW	$gM_W c_{lpha}$	
$H_F Z Z$	$grac{M_Z}{c_W}s_{lpha}$	
H_FWW	$gM_W s_{lpha}$	

TABLE I: Tree-level couplings of the SM-like Higgs boson h and the Flavons H_F and A_F to fermion and gauge boson pairs in the FNSM. Here, $r_s = v/(\sqrt{2}v_s)$, $\cos\alpha(\sin\alpha) \equiv c_\alpha(s_\alpha)$.

C. Model parameter space

A comprehensive analysis of the model parameter space is detailed in Ref. [26]. The only parameters not reported are those that have a direct impact on the observables studied in this work, namely $\tilde{Z}_{e\mu}$ and $\tilde{Z}_{\tau\mu}$. The parameter $\tilde{Z}_{e\mu}$ is constrained most stringently by the radiative decay $\mu \to e\gamma$. For $\tilde{Z}_{\tau\mu}$, we derive limits from the upper bounds on $\mathcal{BR}(\tau \to \mu\gamma)$, $\mathcal{BR}(h \to \tau\mu)$, and $\mathcal{BR}(\tau \to 3\mu)$, with the latter providing the most restrictive constraint.

Figure 1 presents the allowed parameter space for the (a) $\tilde{Z}_{e\mu} - v_s$ and (b) $\tilde{Z}_{\tau\mu} - v_s$ planes. The colored points denote parameter sets consistent with all imposed constraints. We find that the branching ratio $\mathcal{BR}(\mu \to e\gamma)$ imposes the constraint $\mathcal{O}(-10^{-3}) \lesssim \tilde{Z}_{e\mu} \lesssim \mathcal{O}(10^{-3})$, for $v_s \approx 1000$ GeV. Limits on $\tilde{Z}_{\tau\mu}$ are determined by the combined constraints of three observables, restricting it to $\mathcal{O}(-10^{-2}) \lesssim \tilde{Z}_{\tau\mu} \lesssim \mathcal{O}(10^{-2})$ at $v_s \approx 1000$ GeV.

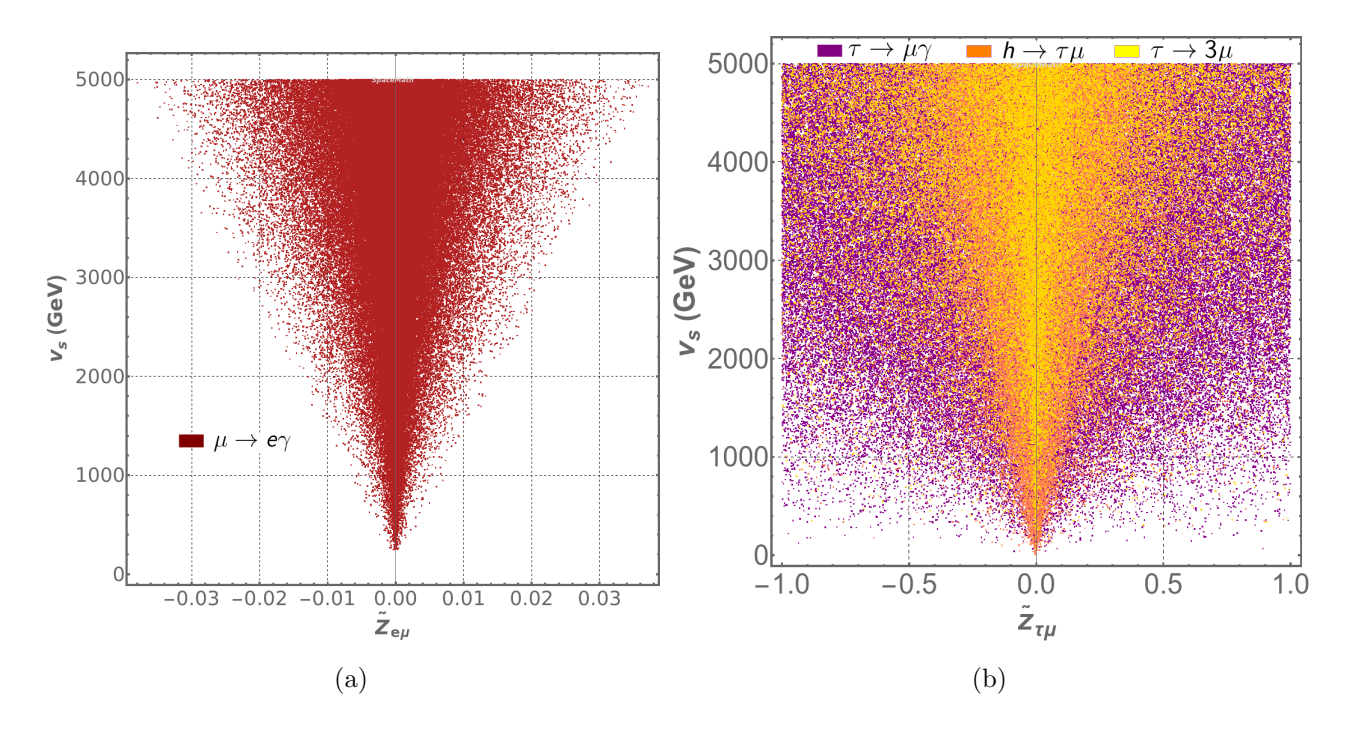


FIG. 1: (a) $Z_{e\mu} - v_s$ plane, and (b) $Z_{\tau\mu} - v_s$ plane. Different colored points correspond to those allowed by upper limits on $\mathcal{BR}(\mu \to e\gamma)$ (cherry), $\mathcal{BR}(\tau \to \mu\gamma)$ (purple), $\mathcal{BR}(h \to \tau\mu)$ (orange), $\mathcal{BR}(\tau \to 3\mu)$ (yellow).

As shown in Fig. 2 of [26], the parameter $\cos \alpha \equiv c_{\alpha}$ is strongly restricted by LHC Higgs boson data, which imposes $c_{\alpha} \gtrsim 0.99$ to prevent significant deviations from the SM $hf\bar{f}$ couplings, see Table I. In light of this, and considering the weak dependence of v_s on c_{α} , we investigate a strict scenario defined by $c_{\alpha} = 0.995$ and $v_s = 1000$ GeV. Consequently, we express our results in the following sections in terms of the flavor-changing parameters $\tilde{Z}_{e\mu}$ and $\tilde{Z}_{\tau\mu}$.

III. COLLIDER ANALYSIS

In this section, we detail the collider analysis for the LFV Higgs decay channels $h \to e\mu$ and $h \to \tau^{\pm}\mu^{\mp}$ ($\tau^{\pm} \to \pi^{\pm}\nu_{\tau}$) in proton-proton collisions. The analysis employs a comprehensive Monte Carlo simulation framework to model both signal and background processes, and utilizing multivariate techniques—specifically Boosted Decision Trees (BDT) machine learning technique—, we achieve separation of the signal from the background.

Signal and background events were simulated with the following chain of stages: we first implement the full model using FeynRules [36] for compatibility with MadGraph5 [37] considering the NNPDF2.3LO parton distribution functions [38]. The generated events are then interfaced with Pythia8 [39] for parton showering and hadronization, followed by detector simulation using Delphes3 [40]. For this purpose, we employ the delphes_card_HLLHC.tcl [41] detector configuration for the HL-LHC.

A. $h \rightarrow e\mu$ Channel

• Signal: This analysis targets the production and cLFV decay of the SM-like Higgs boson, $gg \to h \to e^{\pm}\mu^{\mp}$. Figure 2 shows the signal production cross section, where the blue region denotes the parameter space allowed by the direct experimental limit $\mathcal{BR}(h \to e\mu) < 4.4 \times 10^{-5}$ [23], corresponding to $\tilde{Z}_{e\mu} \lesssim 0.04$. The most stringent constraint from $\mathcal{BR}(\mu \to e\gamma)$ is indicated by the green region, which requires $\tilde{Z}_{e\mu} \lesssim 0.005$ and implies an upper limit of $\sigma(gg \to h \to e\mu) \lesssim 0.00076$ pb. This cross section imposes an upper bound on $\mathcal{BR}(h \to e\mu) \lesssim 1.3 \times 10^{-5}$, which is in accordance with the current limit. For this estimation we use $\sigma(gg \to h) = 58$ pb at $\sqrt{s} = 13.6$ TeV [42].

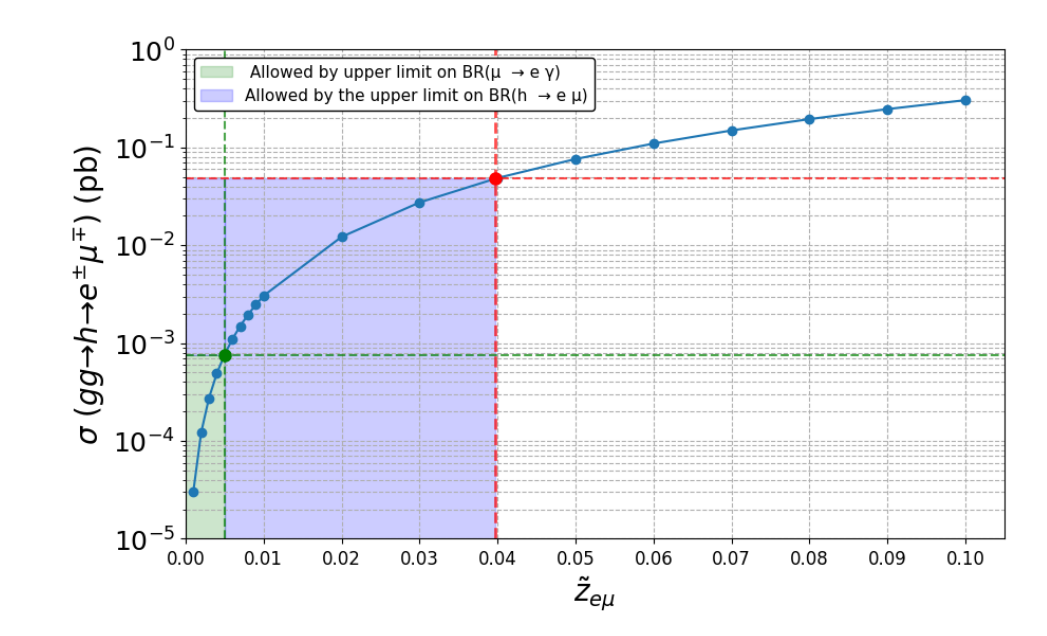


FIG. 2: Production cross section of the signal as a function of $\tilde{Z}_{e\mu}$. The blue area indicates the allowed region by the direct upper limit on $\mathcal{BR}(h \to e\mu)$, while the green zone represents that allowed by the upper bound on $\mathcal{BR}(\mu \to e\gamma)$.

- Background: While SM background processes can yield final states with different-flavor leptons, they originate from mechanisms fundamentally distinct from those involving an explicit lepton-flavor-violating vertex within a single decay. Such backgrounds typically involve undetected neutrinos, manifesting experimentally as missing transverse energy. Consequently, their kinematic distributions—particularly in the region near a resonance in the $e\mu$ invariant mass—deviate significantly from the sharp, two-body decay signature expected from $h \to e\mu$. The dominant background processes contributing to this channel include:
 - Drell-Yan Production: $Z/\gamma^* \to \tau^+\tau^-$ with leptonic tau decays $(\tau \to e\nu_e\nu_\tau, \tau \to \mu\nu_\mu\nu_\tau)$
 - Top Quark Pair Production: $t\bar{t}$ decays yielding opposite-sign $e\mu$ pairs through semileptonic decays

- Diboson Production:
 - * W^+W^- with $W^+ \to e^+\nu_e, W^- \to \mu^-\bar{\nu}_{\mu}$
 - * WZ with $W \to e\nu$, $Z \to \mu\mu$ (one muon missed)
 - * ZZ with both Z bosons decaying leptonically

The production cross sections of the background processes are presented in Table II.

Background Process Cross Section [pb]		
Drell-Yan	26	
Top Quark Production	127.7	
Diboson Production		
$\overline{W^+W^-}$	0.8378	
WZ	0.1364	
ZZ	0.09846	

TABLE II: Cross sections for each background process for $h \to e\mu$.

B.
$$h \to \tau^{\pm} \mu^{\mp} \ (\tau^{\pm} \to \pi^{\pm} \nu_{\tau})$$
 channel

• **Signal:** In this channel, we search for a final state including a charged lepton $\mu = \mu^-, \mu^+,$ a charged pion π^{\pm} and missing transverse energy due to undetected neutrinos: $gg \to h \to \tau^{\pm}\mu^{\mp}$ with $\tau^{\pm} \to \pi^{\pm}\nu_{\tau}$. The signal production cross section as a function of $\tilde{Z}_{\tau\mu}$ is presented in Fig. 3.

As in the previous channel, the blue region denotes the parameter space allowed by the direct experimental limit $\mathcal{BR}(h \to \tau \mu) < 0.0015$ [23], corresponding to $\tilde{Z}_{\tau\mu} \lesssim 0.009$. A more stringent constraint arises from $\mathcal{BR}(\tau \to 3\mu)$, indicated by the green region, which requires $\tilde{Z}_{\tau\mu} \lesssim 0.007$. This value implies an upper limit on the cross section of $\sigma(gg \to h \to \tau \mu) \lesssim 0.00061$ pb, based on $\sigma(gg \to h) = 58$ pb at $\sqrt{s} = 13.6$ TeV [42]. Consequently, the $\tau \to 3\mu$ decay channel sets an indirect upper bound of $\mathcal{BR}(h \to \tau \mu) \lesssim 1 \times 10^{-5}$, which is consistent with the current direct limit and more restrictive by two orders of magnitude.

• Background:

- Drell-Yan Production: Producing $Z/\gamma^* \to \tau^+\tau^-$, which leads to the decay channels:
 - * Leptonic Tau Decays: Leptonic tau decays $\tau \to \ell \nu_\ell \nu_\tau$
 - * Semileptonic Tau Decays: Leptonic tau decays $\tau \to \ell \nu_{\ell} \nu_{\tau}$ and $\tau \to \pi \nu_{\tau}$
 - * Hadronic Tau Decays: Both tau decay hadronically $\tau \to \pi \nu_{\tau}$
- Top Quark Pair Production: $t\bar{t}$ decays yielding muons and jets

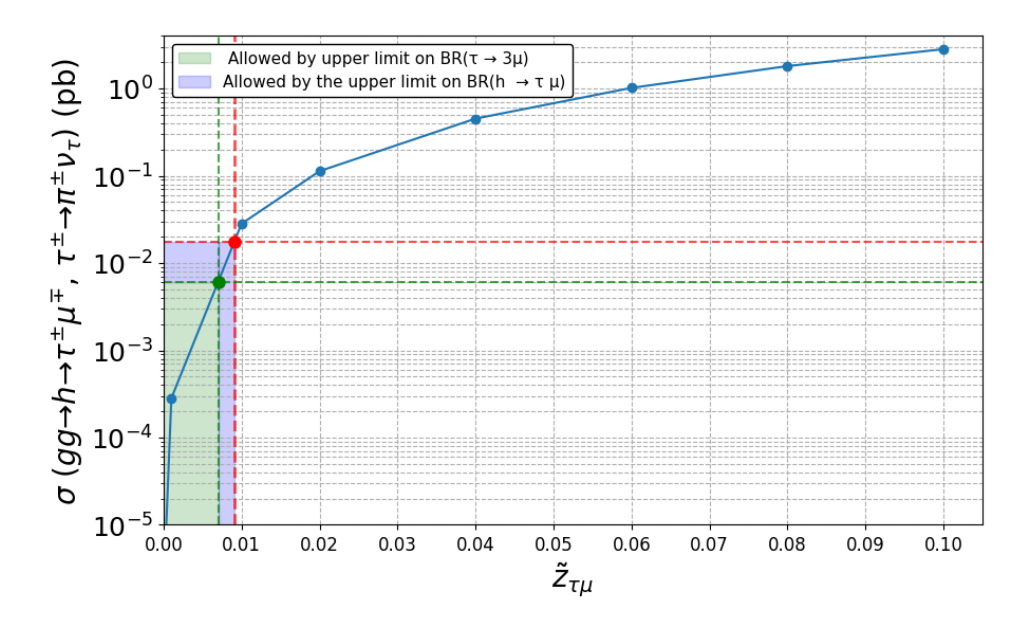


FIG. 3: The blue area indicates the allowed region by the direct upper limit on $\mathcal{BR}(h \to \tau \mu)$, while the green zone represents that allowed by the upper bound on $\mathcal{BR}(\tau \to 3\mu)$.

- WZ: $W \to jet \ jet \ and \ Z \to \ell^+\ell^-$
- Leptonic WW decays: Leptonic W decays $W \to \ell \nu_{\ell} \nu_{\tau}$
- Semileptonic WW decays: One W decays leptonically $W \to \ell \nu_{\ell} \nu_{\tau}$, and the other $W \to jet\ jet$

The production cross sections of the background processes are presented in Table III.

Background Process	Cross Section [pb]		
Top Quark Production	164.80		
Diboson Production			
W^+W^- (leptonic decay)	3.393		
W^+W^- (semileptonic decay)	30.91		
WZ	1.1898		
ZZ	0.09846		
Drell-Yan			
Leptonic Decays	115.57		
Semileptonic Decays	35.51		
Hadronic Decays	10.91		

TABLE III: Cross sections for each background process for $h \to \tau \mu$.

C. Multivariate Analysis

Once the kinematic analysis is completed, we notice that most of the observables used to distinguish the signal from the background have relatively weak discriminating relevance. Thus, we opted to implement selection by determining Multivariate Analysis (MVA) discriminators. These discriminators combine the observables into a single, more powerful classifier. For the MVA training, we use a Boosted Decision Tree (BDT) method [43], implemented via the XG-Boost library [44], using an advanced gradient boosting technique. We trained the BDT classifiers with kinematic observables from the final state particles, including the invariant mass, transverse momentum (p_T) , pseudorapidity (η) , azimuthal angle (ϕ) , the missing transverse energy, angular separation (ΔR) , etc. The BDT training is performed using MC-simulated samples. The signal and background samples are scaled to the expected number of candidates, computed from the integrated luminosity and cross sections. The optimization of the BDT selection is performed separately for each channel to enhance the figure of merit, specifically the signal significance, defined as $S/\sqrt{S+B+(x\cdot B)^2}$. Here, S and B denote the number of signal and background candidates, respectively. The factor x stands for a systematic uncertainty. The main experimental systematic uncertainties considered include the integrated luminosity (1%), lepton identification efficiencies (1.5%), trigger efficiencies (1%), and momentum scale and resolution (0.7%). Theoretical uncertainties account for QCD scale variations (2%), parton distribution functions (1.5%), and background modeling (2%). The multivariate analysis classifier adds an additional 2% uncertainty. These contributions are combined in quadrature, yielding a total systematic uncertainty of 4.36%, consistent with HL-LHC projections for analyses involving well-reconstructed leptonic final states [45].

The BDT model was optimized using the Optuna framework [46], while model performance was evaluated via the Kolmogorov-Smirnov (KS) test. All obtained KS statistics reside within the acceptable [0.05, 1] interval. These results demonstrate that the training procedure successfully avoids overtraining, ensuring generalizable model performance.

D. Results

$h \to e\mu$ channel

Despite experimental challenges, this channel is anticipated to yield a clear signature given sufficient integrated luminosity. Key discriminating observables are the electron and muon transverse momenta (p_T^e and p_T^{μ}), which are predicted to peak at approximately $m_h/2$ GeV in a significant fraction of events, as shown in Fig. 4. The successful measurement of the decay of $h \to \mu\mu$ provides encouragement for the search of $h \to e\mu$ as the coupling of $g_{he\mu} \sim 1.7 \times 10^{-5}$ is only one order of magnitude smaller than $g_{h\mu\mu}$, a disadvantage that could be compensated for by the high luminosity of the HL-LHC.

Figure 5 presents our main results: the signal significance as a function of integrated luminos-

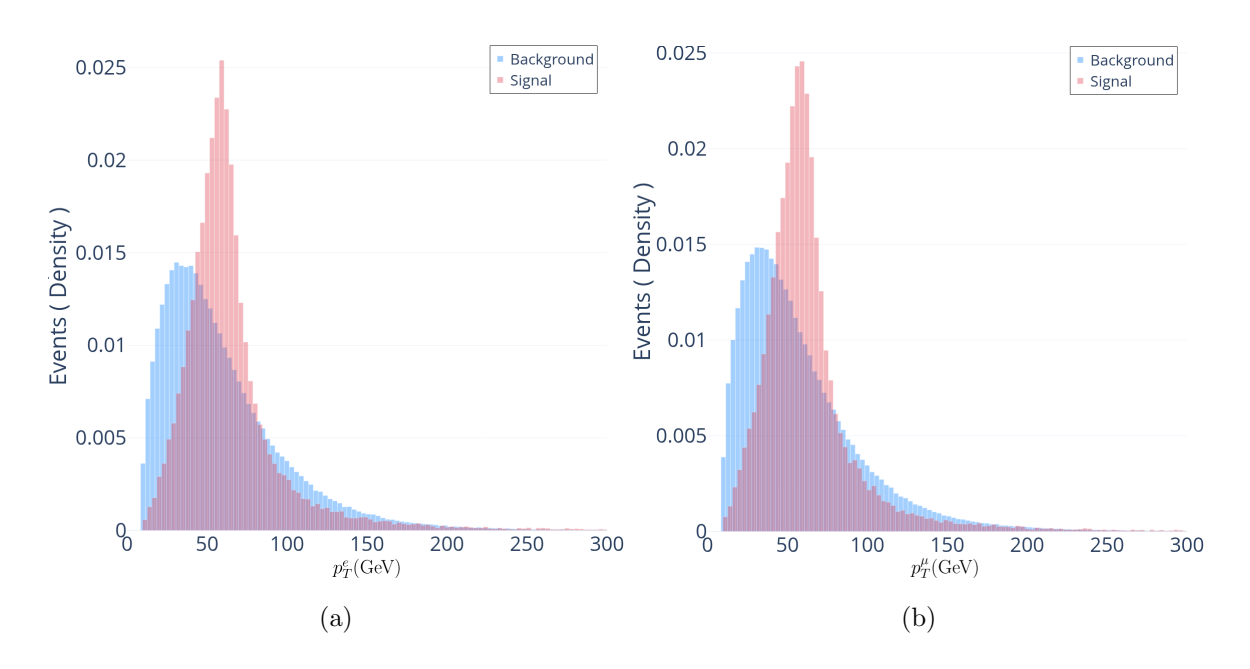


FIG. 4: Kinematical distributions of the most discriminant observables to separate the signal from the background. (a) Transverse momentum of the electron p_T^e , and (b) transverse momentum of the muon p_T^{μ} .

ity for several benchmark cross sections under an XGB cut of 0.995. For the largest cross section considered (7 × 10⁻⁴ pb), the significance exceeds 5σ with an integrated luminosity of approximately 2400 fb⁻¹. This suggests that, after the multivariate selection is applied, the $h \to e\mu$ final state becomes observable at HL-LHC luminosities for cross sections near the upper limit set by the bound on $\mathcal{BR}(\mu \to e\gamma)$. In a less optimistic case, we predict an exclusion limit at 2σ of $\mathcal{BR}(h \to e\mu) < 4.3 \times 10^{-6}$ for $\sigma(gg \to h \to e\mu) = 0.00025$ pb, and an integrated luminosity of 3000 fb⁻¹.

$h \to \tau \mu$ channel

Following the same approach as the previous channel, we present in Fig. 6 the most important observables to separate the signal from the background processes. Meanwhile, Fig. 7 presents the signal significance as a function of integrated luminosity for the $h \to \tau \mu$ channel. The results are shown for several cross section values of $\sigma(gg \to h \to \tau^{\pm}\mu^{\mp}, \tau^{\pm} \to \pi^{\pm}\nu_{\tau})$ under investigation, using an XGB cut of 0.95. Our findings reveal that the HL-LHC could probe this channel with a significance of $\approx 4\sigma$ at an integrated luminosity of 3000 fb⁻¹. Furthermore, a 2σ exclusion limit implies $\mathcal{BR}(h \to \tau \mu) \lesssim 5.2 \times 10^{-5}$ for $\sigma(gg \to h \to \tau \mu) \approx 0.003$ pb and an integrated luminosity of 3000 fb⁻¹.

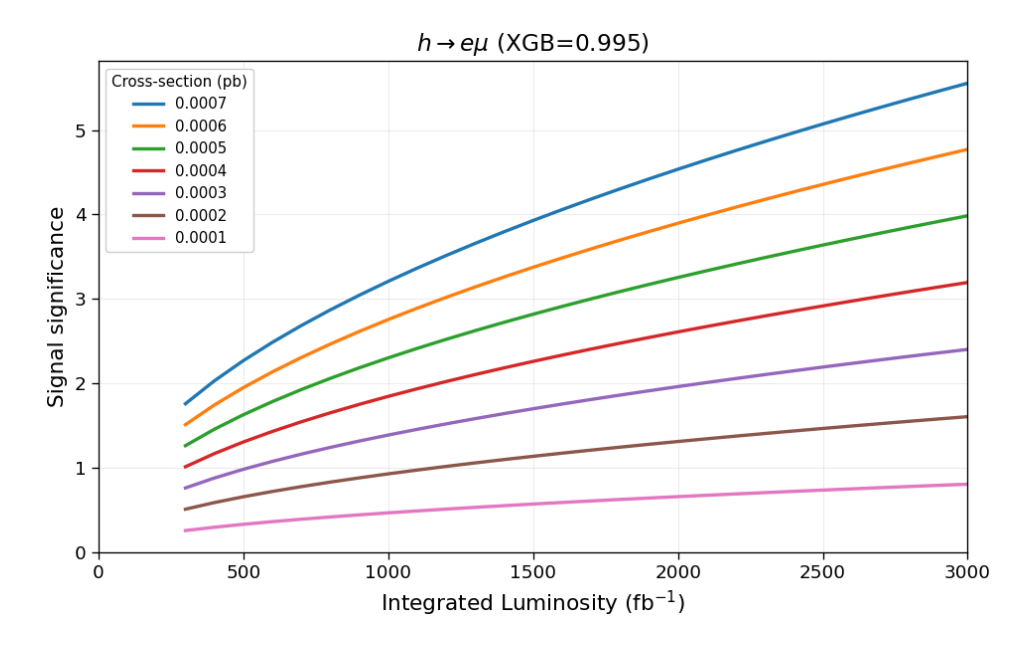


FIG. 5: Signal significance as a function of the integrated luminosity and different cross sections for the $h \to e\mu$ channel, with a cut on XGB of 0.995.

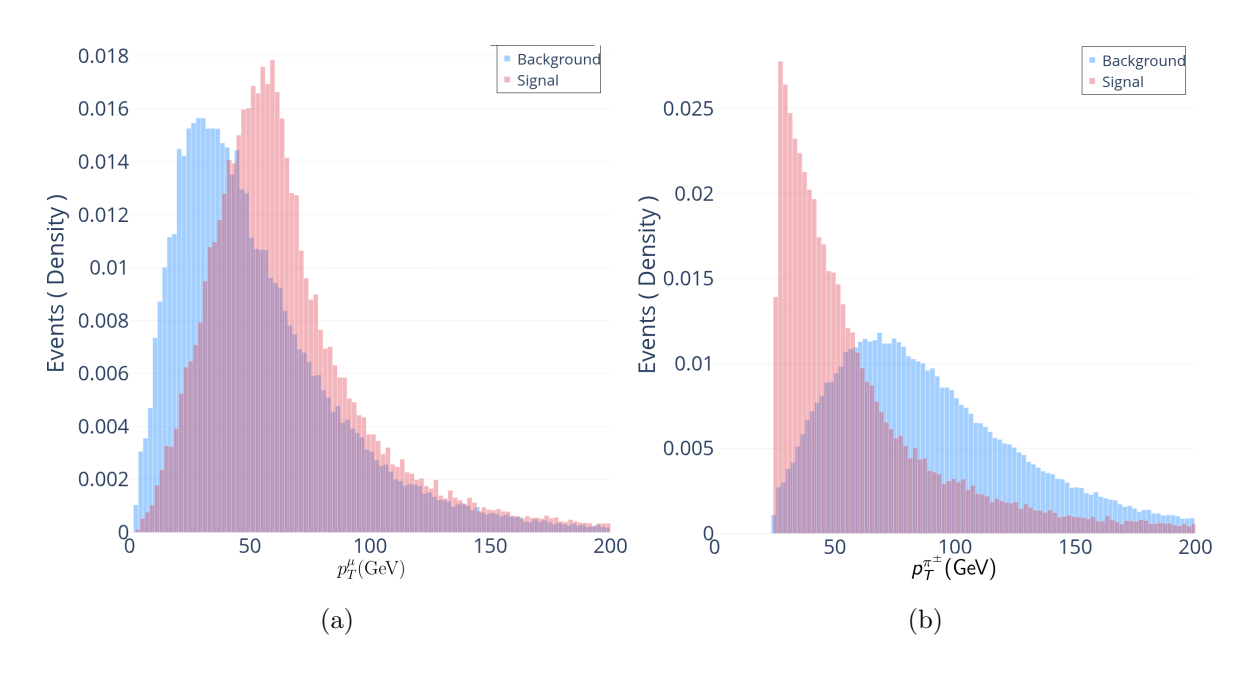


FIG. 6: Kinematical distributions of the most discriminant observables to separate the signal from the background. (a) Transverse momentum of the muon p_T^{μ} , and (b) transverse momentum of the charged pion $p_T^{\pi^{\pm}}$.

$h \to \tau e$ channel

Within the Froggatt-Nielsen model, the $h\tau e$ interaction is directly governed by the $\tilde{Z}_{\tau e}$ coupling. Our analysis of the parameter space reveals that the individual observables— $\tau \to e\gamma$,

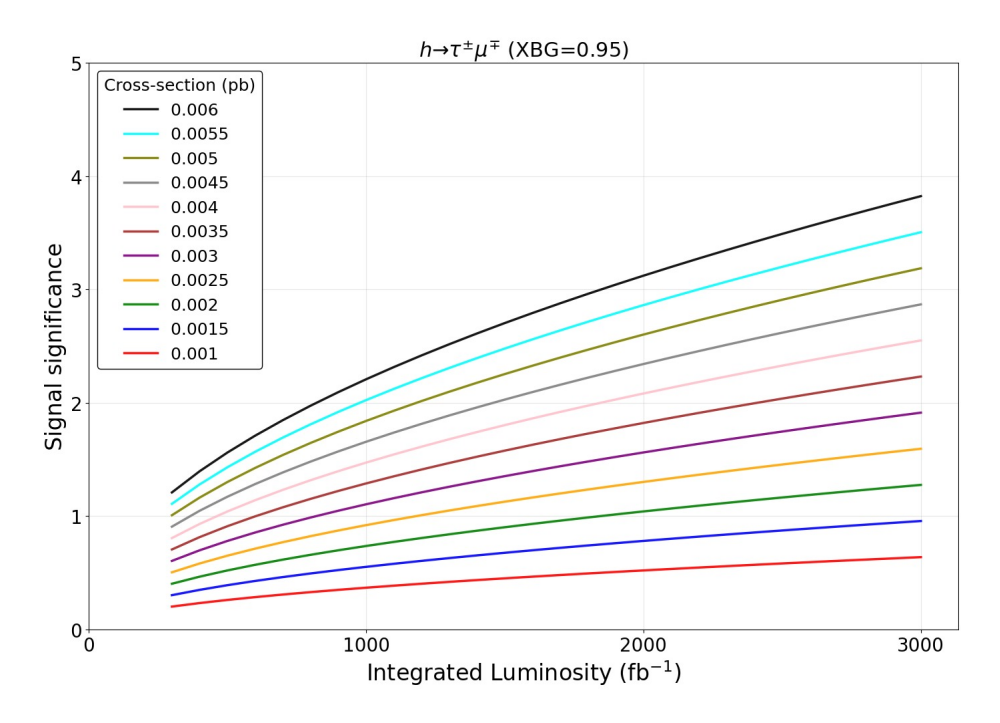


FIG. 7: Signal significance as a function of the integrated luminosity and different cross sections for the $h \to \tau \mu$ channel, with a cut on XGB of 0.95

au ounderrightarrow 3e, and h ounderrightarrow au-are not, on their own, strict enough to impose stringent bounds on $\tilde{Z}_{\tau e}$, which can be as large as $\mathcal{O}(0.1)$. However, a value of this magnitude is unnatural, given that $\tilde{Z}_{\tau \mu}$ and $\tilde{Z}_{e\mu}$ are of the order $\mathcal{O}(10^{-3})$. Motivated by the hierarchy in the quark and lepton sectors, where the CKM and PMNS matrix elements for mixing between the first and third families are smaller than those between the first and second or the second and third, we instead postulate the hierarchy $\tilde{Z}_{\tau \mu} < \tilde{Z}_{e\mu} < \tilde{Z}_{\tau e}$. Using this naturalness argument as a benchmark, we estimate $\tilde{Z}_{\tau e}$ should be less than $\mathcal{O}(10^{-4})$. For a value of $\tilde{Z}_{e\tau} = 0.0005$, we find a cross section of $\sigma(gg \to h \to \tau e, \tau \to \mu \nu_{\mu} \nu_{\tau}) = 9.27 \times 10^{-10}$ pb. This is very small compared to the $h \to e\mu$ and $h \to \tau \mu$ channels, which have cross sections of order 10^{-3} pb. Consequently, the predicted number of events for the τe channel would be significantly smaller and undetectable, even at the integrated luminosity of 3000 fb⁻¹.

IV. CONCLUSIONS

We have presented a study of lepton flavor-violating Higgs boson decays, specifically the $h \to e\mu$ and $h \to \tau^{\pm}\mu^{\mp}$ (with $\tau^{\pm} \to \pi^{\pm}\nu_{\tau}$) channels, at the HL-LHC within the Froggatt-Nielsen model framework. Through a comprehensive collider analysis employing multivariate techniques, we have projected the sensitivity to these rare processes.

Our findings show that the HL-LHC, with its high integrated luminosity, offers the opportunity to probe these LFV decays. For the $h \to e\mu$ channel, a significance exceeding 5σ is attainable with an integrated luminosity of approximately 2400 fb⁻¹ for a cross section of $\sigma(gg \to h \to g)$

 $e\mu$) = 7×10^{-4} pb. The $h \to \tau \mu$ channel can be probed at the $\approx 4\sigma$ level with the full 3000 fb⁻¹ dataset. Furthermore, we have established projected 2σ exclusion limits, implying $\mathcal{BR}(h \to e\mu) \lesssim 4.3 \times 10^{-6}$ and $\mathcal{BR}(h \to \tau \mu) \lesssim 5.2 \times 10^{-5}$ at 3000 fb⁻¹, decreasing by one and two orders of magnitude compared to the current upper limits, respectively. In contrast, for the $h \to \tau e$ channel, our predictions indicate a significantly smaller number of events, rendering this channel undetectable.

The observation of either of these decays would constitute unambiguous evidence for physics beyond the Standard Model. Our results solidify the role of the HL-LHC as a powerful machine for directly testing the fundamental nature of lepton flavor conservation and probing the underlying mechanisms of fermion mass generation.

We encourage experimental collaborations to consider these results. The complete simulation datasets and analysis frameworks are available from the corresponding author upon request.

ACKNOWLEDGMENTS

The work of M. A. Arroyo-Ureña is supported by "Estancias posdoctorales por México (SECI-HTI)", "Sistema Nacional de Investigadoras e Investigadores" (SNII), and the SECIHTI project No. CBF-2025-G-1187. E. A. Herrera-Chacón acknowledges support from SECIHTI. S. Rosado-Navarro thanks VIEP-BUAP for the support.

- [1] M. Raidal et al., Eur. Phys. J. C 57, 13 (2008), arXiv:0801.1826 [hep-ph].
- [2] Q. R. Ahmad et al. (SNO), Phys. Rev. Lett. 89, 011301 (2002), arXiv:nucl-ex/0204008.
- [3] T. Araki et al. (KamLAND), Phys. Rev. Lett. 94, 081801 (2005), arXiv:hep-ex/0406035.
- [4] Y. Ashie et al. (Super-Kamiokande), Phys. Rev. Lett. 93, 101801 (2004), arXiv:hep-ex/0404034.
- [5] M. H. Ahn et al. (K2K), Phys. Rev. D 74, 072003 (2006), arXiv:hep-ex/0606032.
- [6] B. Pontecorvo, Sov. Phys. JETP 6, 429 (1958).
- [7] Z. Maki, M. Nakagawa, and S. Sakata, Prog. Theor. Phys. 28, 870 (1962).
- [8] K. Hayasaka et al., Phys. Lett. B 687, 139 (2010), arXiv:1001.3221 [hep-ex].
- [9] U. Bellgardt et al. (SINDRUM), Nucl. Phys. B 299, 1 (1988).
- [10] A. M. Baldini et al. (MEG), Eur. Phys. J. C 76, 434 (2016), arXiv:1605.05081 [hep-ex].
- [11] B. Aubert et al. (BaBar), Phys. Rev. Lett. **104**, 021802 (2010), arXiv:0908.2381 [hep-ex].
- [12] A. Pilaftsis, Phys. Lett. B **285**, 68 (1992).
- [13] J. G. Korner, A. Pilaftsis, and K. Schilcher, Phys. Rev. D 47, 1080 (1993), arXiv:hep-ph/9301289.
- [14] J. L. Diaz-Cruz and J. J. Toscano, Phys. Rev. D 62, 116005 (2000), arXiv:hep-ph/9910233.
- [15] T. Han and D. Marfatia, Phys. Rev. Lett. 86, 1442 (2001), arXiv:hep-ph/0008141.
- [16] K. A. Assamagan, A. Deandrea, and P.-A. Delsart, Phys. Rev. D 67, 035001 (2003), arXiv:hep-ph/0207302.

- [17] E. Arganda, A. M. Curiel, M. J. Herrero, and D. Temes, Phys. Rev. D 71, 035011 (2005), arXiv:hep-ph/0407302.
- [18] A. Lami and P. Roig, Phys. Rev. D **94**, 056001 (2016), arXiv:1603.09663 [hep-ph].
- [19] M. A. Arroyo-Ureña, J. L. Díaz-Cruz, O. Félix-Beltrán, and M. Zeleny-Mora, Int. J. Mod. Phys. A 39, 2450079 (2024), arXiv:2308.01380 [hep-ph].
- [20] M. A. A. Ureña, R. Gaitan-Lozano, J. H. M. de Oca Yemha, and R. S. Vélez, Rev. Mex. Fis. 67, 040801 (2021).
- [21] M. A. Arroyo-Ureña, T. A. Valencia-Pérez, R. Gaitán, J. H. Montes De Oca, and A. Fernández-Téllez, JHEP 08, 170 (2020), arXiv:2002.04120 [hep-ph].
- [22] G. Aad et al. (ATLAS), JHEP 07, 166 (2023), arXiv:2302.05225 [hep-ex].
- [23] A. M. Sirunyan et al. (CMS), Phys. Rev. D **104**, 032013 (2021), arXiv:2105.03007 [hep-ex].
- [24] A. Cerri et al., CERN Yellow Rep. Monogr. 7, 867 (2019), arXiv:1812.07638 [hep-ph].
- [25] C. D. Froggatt and H. B. Nielsen, Nucl. Phys. B 147, 277 (1979).
- [26] M. A. Arroyo-Ureña, D. Carreño, and T. A. Valencia-Pérez, Phys. Rev. D 111, 115037 (2025), arXiv:2501.18675 [hep-ph].
- [27] M. A. Arroyo-Ureña, A. Chakraborty, J. L. Díaz-Cruz, D. K. Ghosh, N. Khan, and S. Moretti, Phys. Rev. D 108, 095026 (2023), arXiv:2205.12641 [hep-ph].
- [28] M. A. Arroyo-Ureña, J. L. Díaz-Cruz, G. Tavares-Velasco, A. Bolaños, and G. Hernández-Tomé, Phys. Rev. D 98, 015008 (2018), arXiv:1801.00839 [hep-ph].
- [29] M. Bauer, T. Schell, and T. Plehn, Phys. Rev. D 94, 056003 (2016), arXiv:1603.06950 [hep-ph].
- [30] G. Abbas, A. K. Alok, N. R. S. Chundawat, N. Khan, and N. Singh, Phys. Rev. D 110, 115015 (2024), arXiv:2407.09255 [hep-ph].
- [31] M. A. Arroyo-Ureña, A. Fernández-Téllez, and G. Tavares-Velasco, Rev. Mex. Fis. 69, 020803 (2023), arXiv:1906.07821 [hep-ph].
- [32] A. Greljo, A. Smolkovič, and A. Valenti, JHEP 09, 174 (2024), arXiv:2407.02998 [hep-ph].
- [33] E. Loisa and J. Talbert, JHEP 10, 017 (2024), arXiv:2402.16940 [hep-ph].
- [34] S. Kikuchi, T. Kobayashi, and K. Nasu, Phys. Rev. D 109, 115018 (2024), arXiv:2312.11809 [hep-ph].
- [35] P. Asadi, A. Bhattacharya, K. Fraser, S. Homiller, and A. Parikh, JHEP 10, 069 (2023), arXiv:2308.01340 [hep-ph].
- [36] A. Alloul, N. D. Christensen, C. Degrande, C. Duhr, and B. Fuks, Comput. Phys. Commun. 185, 2250 (2014), arXiv:1310.1921 [hep-ph].
- [37] J. Alwall, R. Frederix, S. Frixione, V. Hirschi, F. Maltoni, O. Mattelaer, H. S. Shao, T. Stelzer, P. Torrielli, and M. Zaro, JHEP 07, 079 (2014), arXiv:1405.0301 [hep-ph].
- [38] R. D. Ball et al., Nucl. Phys. B 867, 244 (2013), arXiv:1207.1303 [hep-ph].
- [39] T. Sjöstrand, S. Ask, J. R. Christiansen, R. Corke, N. Desai, P. Ilten, S. Mrenna, S. Prestel, C. O. Rasmussen, and P. Z. Skands, Comput. Phys. Commun. 191, 159 (2015), arXiv:1410.3012 [hep-ph].
- [40] J. de Favereau, C. Delaere, P. Demin, A. Giammanco, V. Lemaître, A. Mertens, and M. Selvaggi

- (DELPHES 3), JHEP **02**, 057 (2014), arXiv:1307.6346 [hep-ex].
- [41] D. Collaboration, *Delphes 3 HL-LHC Card* (2022), gitHub repository: https://github.com/delphes/delphes.
- [42] S. Navas et al. (Particle Data Group), Phys. Rev. D 110, 030001 (2024).
- [43] L. Breiman *et al.*, Classification and regression trees (Wadsworth international group, California, USA, 1984).
- [44] T. Chen and C. Guestrin, in Proc. 22nd ACM SIGKDD Int. Conf. on Knowledge Discovery and Data Mining, KDD '16 (ACM, New York, NY, USA, 2016) p. 785.
- [45] CMS Collaboration, CMS Phase II Upgrade Scope Document, Tech. Rep. CERN-LHCC-2018-019 (CERN, 2018).
- [46] T. Akiba, S. Sano, T. Yanase, T. Ohta, and M. Koyama, in *Proceedings of the 25th ACM SIGKDD International Conference on Knowledge Discovery & Data Mining* (2019) pp. 2623–2631.